Effect of quartic anharmonicity on the carrier transport of cubic halide perovskites $CsSnI_3$ and $CsPbI_3$

Kai-Cheng Zhang [1,*] Chen Shen,[2] Hong-Bin Zhang,[2,†] Yong-Feng Li,[3,4] and Yong Liu[5]
[1]*School of Physical Science and Technology, Bohai University, Jinzhou 121013, China*
[2]*Institute of Materials Science, Technical University of Darmstadt, Alarich-Weiss-Strasse 2, 64287 Darmstadt, Germany*
[3]*School of Science, Inner Mongolia University of Science and Technology, Baotou 014010, China*
[4]*Key Laboratory of Integrated Exploitation of Bayan Obo Multi-Metal Resources, Inner Mongolia University of Science and Technology, Baotou 014010, China*
[5]*State Key Laboratory of Metastable Materials Science & Technology and College of Science, Yanshan University, Qinhuangdao, Hebei 066004, China*

(Received 20 September 2022; revised 13 November 2022; accepted 28 November 2022; published 8 December 2022)

Recent years have witnessed the rising of halide perovskites for potential applications in photovoltaic and optoelectric devices. Due to the tilting motions of the octahedrons and rattling of the filling atoms, cubic halide perovskites show strong anharmonicity and imaginary frequencies in the phonon dispersion, which brings a great challenge to the prediction of carrier transports based on many-body theory. We have investigated the effect of quartic lattice anharmonicity on the carrier transports of cubic $CsSnI_3$ and $CsPbI_3$ in a comparative perspective by first-principles calculations. The hybrid functional of HSE06 was employed to get accurate band gaps and the self-consistent phonon method was used to renormalize interatomic force constants. Based on the electron-phonon Wannier interpolation and Boltzmann transport equation, the carrier mobilities and mode-resolved scattering rates were calculated and the dominant scattering channels were analyzed. Our results reveal that the mobility takes 595.9 and 84.5 cm^2/Vs at room temperature for cubic $CsSnI_3$ and $CsPbI_3$, respectively, in good agreement with the experiment results. The longitudinal stretching mode of the Sn(Pb)-I bond with frequency of 120 cm^{-1} plays a dominant role in carrier scattering. In comparison, the acoustic modes and the rattling modes have a negligible effect on carrier scattering. Calculations of the band scattering rates show that deep valleys emerge at the band edges for both the highest valence band and the lowest conduction band, which is responsible for the slow relaxation of hot carriers. The strength of intraband electron-phonon coupling (EPC) between the band edge and the Sn(Pb)-I bond stretching mode is far larger than those of other modes, which leads to the dominant scattering in carrier transport. Compared with the harmonic approximation of atom interactions, the inclusion of quartic anharmonicity leads to the enhancement of atom interactions, which decreases the EPC strength and consequently increases the carrier mobilities.

DOI: 10.1103/PhysRevB.106.235202

I. INTRODUCTION

Recently, halide perovskites have attracted extensive attention due to the potential application in high-efficiency photovoltaics, laser, and light-emitting diode devices [1–4]. The formula of halide perovskites takes ABX_3 [$A = Cs^+$, formamidinium (FA^+), methylammonium (MA^+); $B = Sn, Pb$; $X = Cl, Br, I$], where the atoms A fill the void formed by the octahedrons BX_6. Due to the rotation of octahedrons BX_6, a phase transition easily occurs as temperature changes in halide perovskites. For instance, when temperature decreases from 673 to 300 K, $CsSnI_3$ sequentially undergoes four phase transitions, i.e., α, β, γ, and Y phases [5]. Theoretical studies reveal that the void space decreases when the octahedrons rotate so that the halide atoms bond to the filling atom more tightly [6,7]. The continuous phase transitions in halide perovskites deteriorate the conversion efficiency of photovoltaics, and therefore it is crucial to anchor the octahedrons by various strategies. Experimentally, by adding large organic ions FA^+ and MA^+ into lead halide perovskites [8] or surface modification [9], the stability of the cubic phase can be greatly improved.

From the perspective of lattice dynamics, the rotation of octahedrons BX_6 will lead to the instability of cubic-phase halide perovskites, which shows the imaginary frequency in the phonon dispersions. The states of cubic halide perovskites are located at the energy saddle point and the systems will experience two energy minima if the atoms are collectively displaced along the eigenvectors of the soft phonon mode [10,11]. Besides the rotation of octahedrons, the filling atoms rattle in the large void surrounded by the octahedrons, which gives rise to a low-frequency rattling mode. Experimental studies indicate that the rattling mode heavily scatters the acoustic phonon and hence contributes to high thermal resistivity [12,13]. These low-frequency optical modes together with acoustic phonon modes couple to the carriers, and

*kczhang@yeah.net
†hzhang@tmm.tu-darmstadt.de

therefore contribute to the mobility of halide perovskites. Experimental measurements reveal that the hole mobility reaches 585 cm^2/Vs for cubic $CsSnI_3$ at room temperature [5], while the mobility only takes 80 cm^2/Vs for cubic $FAPbI_3$ [14]. The big difference in mobilities between halide perovskites presents a big puzzle to the researchers; that is, what dominates in the carrier scattering of halide perovskites? Therefore, it is necessary to explore the origin of the mobility difference between both halide perovskites. In quantum many-body theory, carriers in semiconductors are scattered by phonon via electron-phonon coupling (EPC). However, the emergence of soft modes brings great challenges to the mobility evaluation since carrier scattering is physically meaningful only for a positive frequency phonon.

For halide perovskites at high temperatures, the octahedrons BX_6 tilt frequently from the energy minima and the filling atoms rattle largely in the void cage, which leads to the strengthening of interatomic forces. The renormalization of interatomic forces will stiffen the soft phonon mode and enhance the thermal conductivity, as predicated by theoretical studies [15,16]. Since cubic $CsSnI_3$ and $CsPbI_3$ are strongly anharmonic materials, the thermal renormalization of interatomic forces will strongly modify the phonon dispersion and the EPC matrix, which inevitably affects the carrier transports. Here we study the anharmonic lattice effect on the transport properties of halide perovskites.

Moreover, experiments have observed slow relaxation time of hot carriers for cubic halide perovskites. When electrons of halide perovskites are excited from the valence band to the conduction band by photons, they will lose the energy by coupling to the phonon and eventually relax into the band edge states. Experiments found the relaxation time of 0.4 ps for carriers in $MAPbI_3$, which is much slower than those of organic semiconductors and GaAs films [17–20]. Various mechanisms have been proposed to explain the slow relaxation of hot carriers, i.e., acoustic-optical phonon up-conversion, hot-phonon bottleneck [21], and Auger-heating [22]. However, a direct explanation from numerical calculations is still absent.

In this article, we have investigated the effect of quartic anharmonicity on the carrier transport properties of cubic $CsSnI_3$ and $CsPbI_3$ in the comparative perspective by first-principles calculations. The hybrid functional of HSE06 [23] was used to get an accurate band gap as well as the effective charge mass. The self-consistent phonon calculation was carried out to get the renormalized interatomic force constants (IFCs) and the phonon dispersions. Using the Wannier-Fourier interpolation technique, the EPC matrix was calculated from the renormalized IFCs and the mobilities as well as the mode-resolved scattering rates were calculated by solving the Boltzmann transport equation (BTE), and the calculation results were compared with the experiment results. Based on the calculations of mode-resolved carrier scattering rates and the EPC strengths, the carrier scattering channels were analyzed and the effect of quartic anharmonicity on the carrier transport was discussed. The rest of the article is organized as follows. In Sec. II, we introduce our calculation methods and details. In Sec. III, the calculation results, i.e., carrier mobilities, mode-resolved scattering rates, and EPC strengths, are analyzed and discussed. Finally, the conclusion is given in Sec. IV.

II. METHODS AND CALCULATION DETAILS

A. Method of electron transport calculation

When electrons are driven by an electric field though the perfect crystal of the semiconductor at finite temperature, they will be scattered into new states by the ions vibrating under the equilibrium positions. This leads to the resistivity and carrier mobility at finite temperatures. Within the scheme of BTE, the current density along the α direction can be expressed as [24]

$$\mathbf{J}_\alpha = -\frac{e}{(2\pi)^3}\sum_n \int f_{n\mathbf{k}} v_{n\mathbf{k},\alpha} d\mathbf{k}, \tag{1}$$

where $f_{n\mathbf{k}}$ and $v_{n\mathbf{k}}$ are the Fermi-Dirac distribution and electron velocity, respectively, with the band index n and the momentum $\hbar\mathbf{k}$. Considering $\mathbf{J}_\alpha = \sum_\beta en\mu_{\alpha\beta}E_\beta$, the electron mobility can be expressed as the derivative of $\mathbf{J}_\alpha$ with respect to the electric field,

$$\mu^e_{\alpha\beta} = -\frac{\sum_{n\in \mathrm{CB}} \int v_{n\mathbf{k},\alpha}\partial_{E_\beta} f_{n\mathbf{k}} d\mathbf{k}}{\sum_{n\in \mathrm{CB}} \int f^0_{n\mathbf{k}} d\mathbf{k}}. \tag{2}$$

The contribution to $\partial_{E_\beta} f_{n\mathbf{k}}$ comes from two parts, i.e., the drift of $f_{n\mathbf{k}}$ under the electric field as well as the excitations of electrons and holes by colliding with ions. In a small electric field, i.e., $eE_\beta \ell_\beta \ll k_B T$ (ℓ_β is the mean free path of the electron), the excitation of the electron and holes from the Fermi sphere can be neglected and the electron mobility can be solved by integration under self-energy relaxation time approximation [25] (SERTA). The k-dependent scattering rate, $\gamma_{n\mathbf{k}} = 1/\tau^0_{n\mathbf{k}}$, can be derived from Fan-Migdal electron self-energy as follows [25]:

$$\begin{aligned}\frac{1}{\tau^0_{n\mathbf{k}}} = \frac{2\pi}{\hbar}\sum_{m\nu}\int \frac{d\mathbf{q}}{\Omega_{\mathrm{BZ}}} |g_{mn\nu}(\mathbf{k},\mathbf{q})|^2 \\ \times \left[\left(1 + n_{\mathbf{q}\nu} - f^0_{m\mathbf{k}+\mathbf{q}}\right)\delta(\varepsilon_{n\mathbf{k}} - \varepsilon_{m\mathbf{k}+\mathbf{q}} - \hbar\omega_{\mathbf{q}\nu}) \right. \\ \left. + \left(f^0_{m\mathbf{k}+\mathbf{q}} + n_{\mathbf{q}\nu}\right)\delta(\varepsilon_{n\mathbf{k}} - \varepsilon_{m\mathbf{k}+\mathbf{q}} + \hbar\omega_{\mathbf{q}\nu})\right].\end{aligned} \tag{3}$$

In the above equation, $g_{mn\nu}(\mathbf{k},\mathbf{q})$ is the matrix element of EPC, which represents the probability amplitude of electron scattering from the state $|n\mathbf{k}>$ to $|m\mathbf{k}+\mathbf{q}>$ by absorbing a phonon of $|\mathbf{q}\nu>$. It can be calculated by the following equation:

$$g_{mn\nu}(\mathbf{k},\mathbf{q}) = \sqrt{\frac{\hbar}{2M\omega_{\mathbf{q}\nu}}}\left\langle n\mathbf{k}\left|\frac{\partial V_{KS}}{\partial u_{\mathbf{q}\nu}}\right|m\mathbf{k}+\mathbf{q}\right\rangle, \tag{4}$$

where M and $\omega_{\mathbf{q}\nu}$ are the mass of the unit cell and the angular frequency of phonon $|\mathbf{q}\nu>$. $\frac{\partial V_{KS}}{\partial u_{\mathbf{q}\nu}}$ is the deformation potential with respect to the displacement of phonon $|\mathbf{q}\nu>$, which can be calculated by the density functional perturbation theory (DFPT) [26].

To obtain accurate carrier mobilities, the Wannier-Fourier interpolation technique was used to evaluate Eqs. (2) and (3) with very dense $k(q)$ mesh, as implemented in the EPW code [27]. This technique first transforms the Hamiltonian, dynamical matrix, and EPC matrix elements into the Wannier representation by maximally localized Wannier functions [28] with coarse $k(q)$ mesh, and then transforms them back to the Bloch representation with very fine $k(q)$ mesh. So the mobility can be calculated more accurately provided that the

eigenvalues of the electron, phonon frequencies, and EPC matrix elements have been given by interpolation. The long-range dipolar interaction arising from Born effective charges together with the dielectric constants have also been included in the EPC calculation. Note that in the calculation of EPC matrix elements, the imaginary frequency of the harmonic phonon will be truncated to guarantee that the corresponding carrier scattering is physically meaningful. We set the coarse q and k mesh to be $4 \times 4 \times 4$ and $8 \times 8 \times 8$ for the calculations of the phonon and electron eigenvalues, respectively. A fine mesh of $40 \times 40 \times 40$ was used to achieve the convergent results. The carrier density in the halide perovskites was set to be $10^{17} e/\mathrm{cm}^3$.

B. Method of self-consistent phonon calculation

In a perfect crystal, the ions vibrate in the equilibrium positions and the potential energy can be expanded to a Taylor series of atomic displacements. If the potential well is parabolic, the vibration is harmonic and the dispersion can be solved provided that the dynamical matrix is given. For the crystal of strong anharmonicity, the cubic and quartic terms of potential expansions must be included, which will modify the phonon linewidth and frequencies, respectively. Higher-order potential expansions are generally neglected due to their trivial contribution to the energy, as verified by the thermal conductivity calculations of several anharmonic compounds [16,29]. In many-body Green's function theory, the anharmonic terms can be treated as the self-energy to the free phonon Green's function $G_q^0(\omega)$. By solving the Dyson equation, $[G_{\mathbf{q}}(\omega)]^{-1} = [G_{\mathbf{q}}^0(\omega)]^{-1} - \Sigma_{\mathbf{q}}(\omega)$, the renormalized frequency Ω_q without polarization mixing can be written as [29]

$$\Omega_q^2 = \omega_q^2 + 2\Omega_q I_q(\Omega_q), \tag{5}$$

$$I_q(\Omega_q) = \frac{1}{2}\sum_{q'} \frac{\hbar\Phi(q,-q,q',-q')}{4\Omega_q\Omega_{q'}}[1+2n(\Omega_{q'})], \tag{6}$$

where $\Phi(q,-q,q',-q')$ are the quartic IFC, and $n(\Omega_q)$ is the Bose-Einstein distribution function. The renormalized frequency can be given by solving Eq. (5) iteratively, which is called the self-consistent phonon (SCPH) method [29,30].

In principle, the cubic and quartic IFCs can be calculated by the finite-difference approach, which generates the configurations with irreducible displacements of atoms for density functional theory (DFT) calculations. However, due to the rapid increase of irreducible configurations for higher-order IFCs, the finite-difference approach is very computationally expensive. Alternatively, we use the method of compressive sensoring lattice dynamics [31] to estimate the anharmonic IFC. The *ab initio* molecular dynamics (AIMD) of the Car-Parrinello method [32] was used to simulate the thermal equilibrium states of system with the size of $2 \times 2 \times 2$. The Nose-Hoover thermostats [33] were used to stabilize the temperature of the canonical ensemble at 430 K. The total simulation time lasts for 12 ps, with the time step of 2 fs to update the configuration. The former 6 ps was used to achieve the thermal equilibrium state and the latter 6 ps was used for randomly sampling 160 configurations. The atoms of the sampled configurations were displaced by 0.1 Å along random directions. After self-consistent DFT calculations, the sparse solution of the displacement-force sets was solved by the least absolute shrinkage and selection operator (LASSO) technique [29] with the cutoff radius of quartic IFC set to be 7.4 Å. The effect of Fock exchange on IFC was not included since IFC is less sensitive to the band-gap variation. By the SCPH method, the renormalized harmonic IFC as well as the dynamical matrix can be obtained, which is used for further calculations of the EPC matrix. Hence, the effect of quartic lattice anharmonicity is naturally included in the EPC matrix.

C. Details of density functional calculation

We carried out the study on the electronic structures and transport properties of halide perovskites by first-principles calculations based on the plane-wave method, as implemented in the QUANTUM ESPRESSO (QE) computing package [34]. Full-relativistic optimized norm-conserving Vanderbilt (ONCV) pseudopotentials of the Perdew-Burke-Ernzerhof (PBE) form [35,36] were used for the elements of Cs, Sn, Pb, and I, with the shell configurations of $5s^2p^66s^1$, $4d^{10}5s^2p^2$, $5d^{10}6s^2p^2$, and $5s^2p^5$, respectively. The plane waves were expanded up to 70 Ry, and the criterion of 10^{-9} Ry was used for energy convergence. The k mesh of $15 \times 15 \times 15$ was used for the energy integration of the PBE calculations. The hybrid functional of HSE06 [23], together with the optimized fraction of Fock correlation 0.17 (0.24) for $CsSnI_3$ ($CsPbI_3$) and k mesh of $8 \times 8 \times 8$, was used to achieve the band gap close to the experimental results.

III. RESULTS AND DISCUSSION

A. Electronic and phonon dispersions

The cubic phase of halide perovskites $CsSnI_3$ ($CsPbI_3$) has the space group of $Pm\bar{3}m$ (No. 221) with three irreducible Wyckoff positions (0,0,0), (1/2, 1/2, 1/2), and (0,1/2,1/2) occupied by one Cs, one Sn (Pb), and three I atoms. The Sn (Pb) atom is bonded to six nearest-neighbor I atoms, which forms the octahedral SnI_6. Cs donates one 6s electron completely and weakly bonds to the cage of the connected SnI_6. We carried out density functional calculations on the band structures of halide perovskites by including spin-orbital coupling (SOC). As shown in Figs. 1(a) and 1(b), $CsSnI_3$ and $CsPbI_3$ of the cubic phase belong to the semiconductors of the direct band gap, with the valence band maximum (VBM) and conduction band minimum (CBM) located at the R point of the Brillouin zone. The conduction bands are mainly contributed from the 5p (6p) orbits of Sn (Pb) and 6s orbits of I, while the valence bands consist of the 5p orbits of I and 5s (6s) orbits of Sn (Pb). It is found that the PBE functional significantly underestimates the band gap of halide perovskites since E_g only takes 0.06 and 0.20 eV for $CsSnI_3$ and $CsPbI_3$, respectively, which are far less than the experimental values of 1.3 and 1.8 eV [5]. Therefore, we used the hybrid functional [23] of HSE06 to improve the band-gap calculations. In Figs. 1(a) and 1(b), the band gaps have been improved to 1.15 and 1.86 eV for $CsSnI_3$ and $CsPbI_3$, in good agreement with the experiment values.

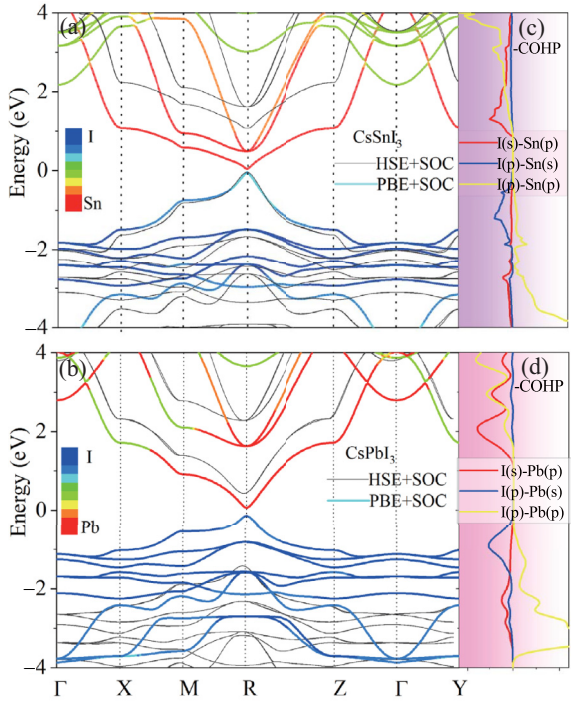

FIG. 1. (a),(b) Band structures of the cubic phase (a) $CsSnI_3$ and (b) $CsPbI_3$ calculated by PBE + SOC (color mapped) and HSE + SOC (gray), respectively. The p orbits of the Sn (Pb) and I atoms are weighted by color mapping to the conduction and valence bands, respectively. The Fermi level is set to be zero. (c),(d) Chemical bonding of orbital pairs for (c) Sn-I and (d) Pb-I in the halide perovskites.

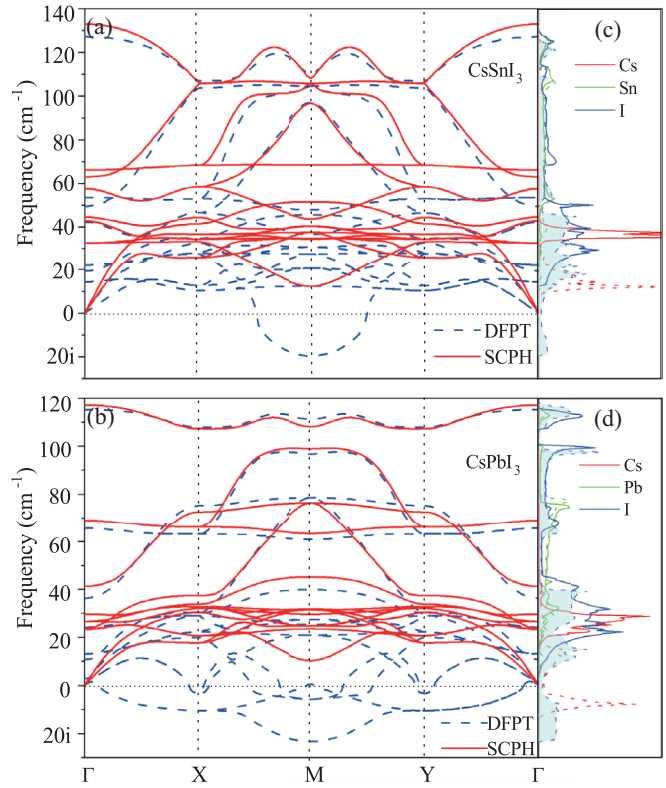

FIG. 2. (a),(b) Phonon dispersions for (a) $CsSnI_3$ and (b) $CsPbI_3$. The dotted and solid lines represent the harmonic and anharmonic dispersions calculated by the DFPT and SCPH methods, respectively. The anharmonic dispersions were calculated by SCPH for both halide perovskites at 400 K. (c),(d) Atom-projected density of states (PDOS) for (c) $CsSnI_3$ and (d) $CsPbI_3$, respectively. The shaded areas represent the PDOS of the I atoms calculated by DFPT.

To analyze the chemical bonding of the band edges, we carried out the calculations on the projected crystal orbital Hamiltonian population [37] (COHP) for both halide perovskites. Figure 1(c) shows that the conduction band edge arises from the antibonding states between 6s of I and 5p of Sn, while the valence band edge is mainly contributed by the antibonding states between 5p of I and 5s of Sn. It is found that the bonding and antibonding states between the 5p orbits of I and Sn are far beneath and above the Fermi level, respectively. Similar bonding states occur to $CsPbI_3$, as shown in Fig. 1(d).

By fitting the band edges to the parabolic function, the effective mass of carriers, $m^{\star}_{h(e)}$, can be derived. Fitting of PBE + SOC band structures reveals that $m^{*}_{h(e)}$ is spatially isotropic for both halide perovskites and it gives $m^{*}_{h} = m^{*}_{e} = 0.022$ for $CsSnI_3$ and $m^{*}_{h} = m^{*}_{e} = 0.053$ for $CsPbI_3$. When the Fock correlation is included, the band gap is further enlarged by enhanced Coulomb repulsion from the p orbits, which reduces the dispersion at the band edge. As expected, m^{*}_{h} (m^{*}_{e}) increases to 0.078 (0.105) for $CsSnI_3$, and 0.131 (0.120) for $CsPbI_3$, as listed in Table I. Since m^{*}_{h} of $CsPbI_3$ is about twice the effective hole mass of $CsSnI_3$, the much smaller mobility of the former cannot be attributed to the band velocity.

Figure 2 shows the phonon dispersions of halide perovskites calculated by both the DFPT and SCPH methods. The anharmonic phonon dispersions have been calculated by the SCPH method at 400 K. As shown in Fig. 2(a), large imaginary frequencies are found at the R point for the harmonic dispersion of $CsSnI_3$. These imaginary-frequency modes arise from the rotating instability of octahedrons SnI_6 around the c crystal axis since the projected density of states (PDOS) of I spans to the imaginary-frequency region, as shown in Fig. 2(c). Polarization corrections were also included in the

TABLE I. Calculation results of halide perovskites. E_g(PBE) and E_g(HSE), in units of eV, are the band gaps calculated by the PBE and HSE functionals with SOC interaction. The effective carrier mass, $m^{*}_{h(e)}$, takes the unit of the electron static mass. Hole (electron) mobility $\mu_{h(e)}$ and relaxation time $\tau_{h(e)}$ are in units of cm^2/Vs and fs. ε and Z^* are the static dielectric constant and Born effective charge (in units of e), respectively. $Z_I^{*\parallel}$ and $Z_I^{*\perp}$ denote the Born effective charge of I along and perpendicular to the Sn-I bond, respectively.

	E_g(PBE)	E_g(HSE)	m^{*}_{h}	m^{*}_{e}	μ_h	μ_e	τ_h	τ_e	ε	Z^{*}_{Cs}	$Z_I^{*\parallel}$	$Z_I^{*\perp}$	$Z^{*}_{Sn/Pb}$
$CsSnI_3$	0.06	1.15	0.105	0.078	595.9	239.9	29.7	19.3	7.92	1.38	−5.41	−0.81	5.78
$CsPbI_3$	0.20	1.86	0.120	0.131	84.5	125.3	11.1	12.9	6.82	1.38	−4.95	−0.84	5.31

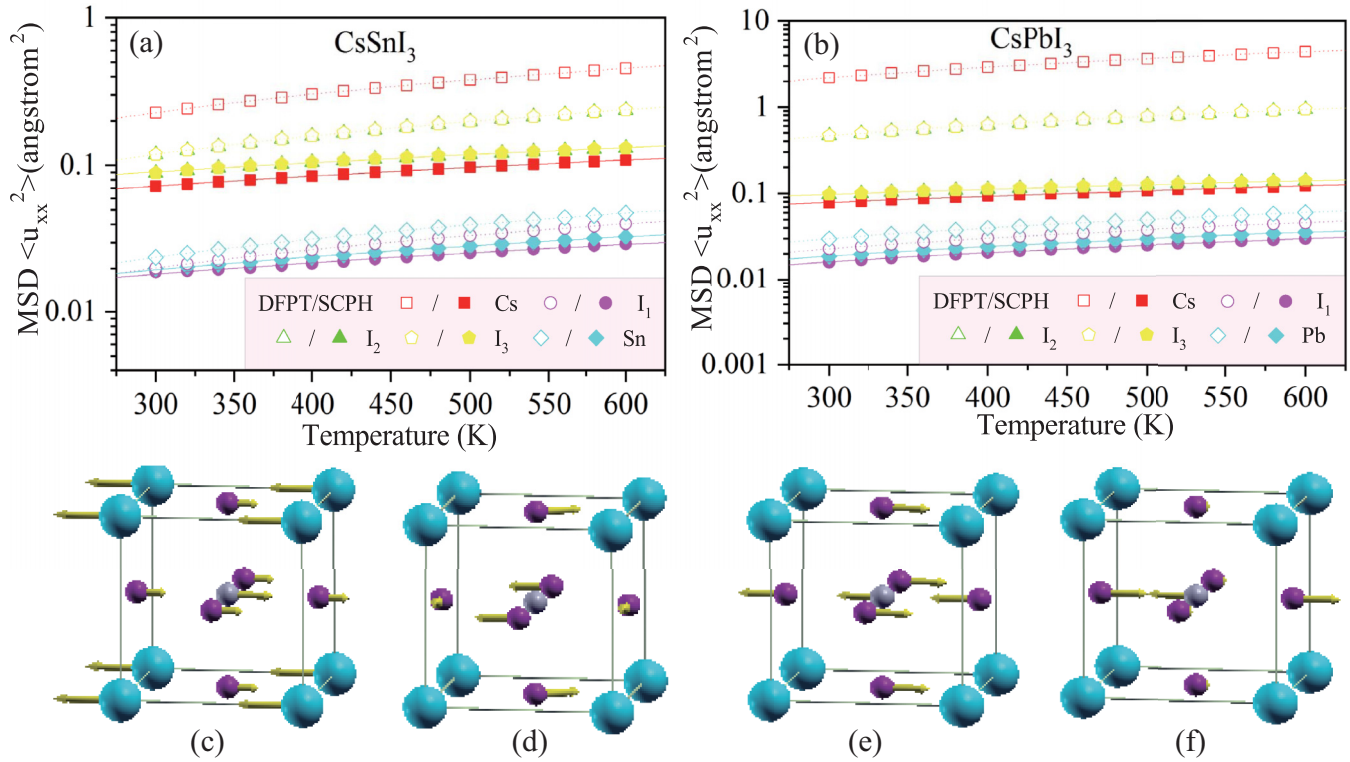

FIG. 3. (a),(b) Mean-square displacements $< u_{xx}^2 >$ of irreducible atoms for (a) $CsSnI_3$ and (b) $CsPbI_3$. I_1, I_2, and I_3 atoms bond to the center Sn atom from the directions of x, y, and z, respectively. Open and solid symbols display the results of DFPT and SCPH, respectively. Data points are fitted linearly. (c)–(f) Atom displacements of phonon modes (c) LO_1, (d) LO_2, (e) LO_3, and (f) LO_4 in the center of the Brillouin zone. Cyan, magenta, and gray spheres represent Cs, I, and Sn(Pb) atoms, respectively.

phonon calculations by considering the dipolar interactions between the Born effective charges. Large longitudinal optical (LO) and transverse optical (TO) phonon splitting occurs to the modes T_{1u} of which the LO branch shifts from 56.9 to 125.8 cm^{-1}, due to the macroscopic electric field in polar materials. Also, flat phonon bands around 10 cm^{-1} can be attributed to the rattling modes of Cs, which corresponds to a PDOS peak. For $CsPbI_3$, the imaginary-frequency modes come from the motions of I and Cs, as shown in Figs. 2(b)–2(d). LO-TO splitting has pushed the longitudinal T_{1u} mode to 115.7 cm^{-1}. When the quartic anharmonicity is included, the interatomic forces between Cs and I have been strengthened. Consequently, the low-frequency modes related to the I and Cs atoms have been stiffened to 30 and 36 cm^{-1} for $CsSnI_3$. Similar frequency stiffening has also occurred to $CsPbI_3$. It is noticed that frequency renormalization mainly occurs to those phonon modes with frequency below 20 cm^{-1}, namely, the rotating modes of octahedrons and the rattling modes of Cs, while those modes with high frequencies have been less stiffened.

Further, we calculated the mean-square displacements (MSDs) of atoms for the halide perovskites by both harmonic and anharmonic approximations, as shown in Figs. 3(a) and 3(b). In the harmonic approximation, the soft phonon modes are truncated to ensure MSDs only come from the modes with positive frequency. Under the cubic point symmetry, the MSD is spatially isotropic for the Cs and Sn atoms, i.e., $< u_{xx}^2 >=< u_{yy}^2 >=< u_{zz}^2 >$, while it reduces to be anisotropic for I atoms in the directions parallel and perpendicular to the Sn-I bond, i.e., $< u_{\parallel}^2 > \neq < u_{\perp}^2 >$, due to the local bonding of Sn, as shown in Fig. 3(a). Under harmonic approximation, MSD takes 0.380 and 0.040 $Å^2$ for Cs and Sn at 500 K, while it takes 0.034 and 0.198 $Å^2$ for I atoms along and perpendicular to the Sn-I bond. The larger MSD of Cs means that it locates in the flatter potential well and prefers to rattling motion in the void cage. In contrast, Sn has much smaller MSD due to its covalence bonding to I. It is found that the I atom has strong anisotropic MSD, indicating a preferable distortion of octahedron SnI_6. By considering the quartic anharmonicity, MSD has significantly reduced for Cs and I atoms because of the renormalization of the interatomic forces. For instance, it takes 0.097 and 0.029 $Å^2$ for Cs and Sn atoms, and 0.026 and 0.119 $Å^2$ for I atoms parallel and perpendicular to the Sn-I bond, which is close to the experimental values [5] (Cs: $U_{11} = 0.154$ $Å^2$; Sn: $U_{11} = 0.049$ $Å^2$; I: $U_{11} = 0.040$, $U_{22} = 0.215$ $Å^2$) [5]. As the temperature increases, the MSD increases linearly. For $CsPbI_3$, the calculation of the DFPT gives an even larger MSD than that of $CsSnI_3$, as shown in Fig. 3(b). When the quartic anharmonicity is considered, the thermal displacements are reduced significantly, i.e., 0.120 and 0.035 $Å^2$ for Cs and Pb, respectively, as well as 0.030 and 0.139 $Å^2$ for I atoms at 600 K, which is close to the experimental results [38] (Cs: $U_{11} = 0.182$ $Å^2$; Pb: $U_{11} = 0.058$ $Å^2$; I: $U_{11} = 0.035$, $U_{22} = 0.282$ $Å^2$).

In the charge transports of semiconductors, the longitudinal phonon usually scatters carriers heavily via EPC. By analyzing the collective motions of phonon modes at the Γ point, we find that five longitudinal modes dominate in halide

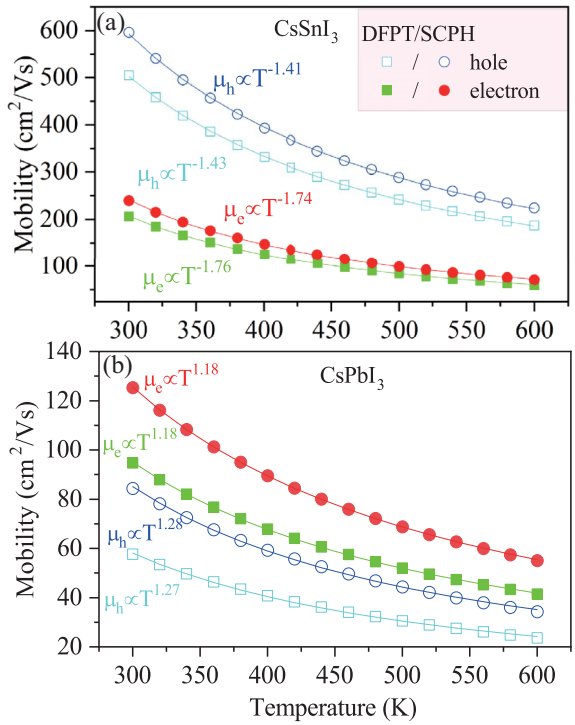

FIG. 4. Carrier mobilities calculated by the BTE method for (a) $CsSnI_3$ and (b) $CsPbI_3$, respectively. Data are fitted according to the power law. Carriers are scattered by the phonon with both harmonic (DFPT) and anharmonic (SCPH) approximations.

perovskites, namely, one acoustic mode and four optical modes, as shown in Figs. 3(c)–3(f). As can be seen, LO_1 represents the rattling motion of Cs relative to SnI_6. LO_2 and LO_3 mainly characterize the distortion of SnI_6, while the LO_4 mode represents the stretching motion of the Sn-I bond. The frequency at the Γ point takes 32.5 (23.7), 42.9 (26.5), 59.0 (41.3), and 131.7 (117.2) cm^{-1} as the mode counts from LO_1 to LO_4 for $CsSnI_3$ ($CsPbI_3$). Compared to other LO modes, the LO_4 mode has the largest frequencies in the phonon dispersion. We will discuss the effect of these phonon modes on carrier scattering in the subsequent sections.

B. Mobility and relaxation time

In order to investigate the anharmonicity effect of the phonon on the charge transport, we calculated the EPC matrix elements by Eq. (4), for which the eigenvectors of the electrons were calculated by hybrid functionals, while the eigenvectors and eigenvalues of the phonon were calculated by both the DFPT and SCPH methods. After interpolating the EPC matrix to fine q and k mesh of size $40 \times 40 \times 40$, the carrier mobilities were calculated by solving BTE with SERTA.

For $CsSnI_3$, carriers scattered by the anharmonic phonon have larger mobilities than those scattered by the harmonic phonon, as shown in Fig. 4(a). At 300 K, mobility takes 595.9 cm^2/Vs for holes scattered by the anharmonic phonon, in good agreement with the experiment result (585 cm^2/Vs) [5]. In contrast, the mobility of holes scattered by the harmonic phonon takes 505.1 cm^2/Vs, indicating an overestimated scattering of carriers. As the temperature increases, the mobilities decay by following the power law $\mu = aT^{-\alpha}$, where α takes 1.41 and 1.74 for the hole and electron, respectively. For cubic $CsPbI_3$, our results reveal that electron carriers have larger mobility than hole carriers, i.e., $\mu_e = 125.3$ and $\mu_h = 84.5$ cm^2/Vs at 300 K, as shown in Fig. 4(b). Recent experiments have verified that the electron mobility is much higher than the hole mobility for cubic $CsPbI_3$ [39], and our result is consistent with the experiment measurements. Transport experiments reveal that μ_h takes ∼10–30 cm^2/Vs for cubic phase $CsPbI_3$ [40–42], ∼38–40 cm^2/Vs for $MAPbI_3$ [43,44], and 80cm^2/Vs for $FAPbI_3$ [14]. Also, a DFT calculation predicts that the upper limit of the hole mobility takes 80 cm^2/Vs for cubic $CsPbI_3$ at room temperature [45], which is in good agreement with our results. For $CsPbI_3$, the exponent α takes 1.28 and 1.18 for hole and electron carriers, respectively. The exponent α is found to be nearly the same for carriers scattered by harmonic and anharmonic phonons. It is well known that the exponent α will take 1.5 when the acoustic phonon dominates in the carrier scattering. Recently, transport experiments on halide perovskites have reported that the exponent α takes 1.5 for $MAPbI_3$ [46,47], ∼1.46–1.5 for cubic $MAPbBr_3$ and $CsPbBr_3$ [48,49], as well as ∼1.54–2.04 for lead halide perovskites nanowires [50]. Our fitting exponents are close to the experiment results. Although bulk halide perovskites of the cubic phase are not energetically favored at room temperature, they can survive in nanowires [51] or thin films [52] for a long time. Nevertheless, the continuous transition to orthorhombic phases enlarges the band gap and the effective mass of carriers [53], which inevitably lowers the carrier mobility.

In the EPC picture, the relaxation time τ characterizes the timescale in which carriers are scattered into other states by the phonon. The electric conductivity is related to the relaxation time by the equation $\sigma = ne^2\tau/m^*$. Large τ usually means good electric conductivity. The electron relaxation time τ_e can be calculated via the equation $\tau_e = \sum_k \tau_k f_k / \sum_k f_k$, where τ_k is the k-dependent relaxation time and f_k is the distribution function. For hole carriers, the relaxation time τ_h can be obtained by replacing f_k to $1 - f_k$. The relaxation time has been calculated for both halide perovskites by considering the carrier scattering arising from harmonic and anharmonic phonons, as shown in Fig. 5. As temperature increases, the decay of relaxation time can be well fitted in the power law $\tau = ae^{-\beta}$. The exponent β takes ∼1.09–1.10 and ∼1.25–1.27 for hole and electron carriers of $CsSnI_3$, respectively, as shown in Fig. 5(a). In comparison to $CsSnI_3$, the exponent β remains to be 1.09 for hole carriers, while it decreases to 1.11 for electron carriers, as shown in Fig. 5(b). When carriers are scattered by the anharmonic phonon, the decay exponent is found to be nearly unchanged, while the relaxation time is enhanced significantly for both halide perovskites. At 300 K, τ_h of $CsSnI_3$ increases from 25.3 to 29.7 fs after the renormalization of interatomic forces. Similarly, τ_h of $CsPbI_3$ is enhanced from 7.4 to 11.1 fs due to the strengthened interatomic bonding.

C. Mode-resolved scattering rates

Usually, carriers in semiconductors are predominantly scattered by LA and LO modes, which heavily contributes to resistivity. The LA mode causes the volume variation of

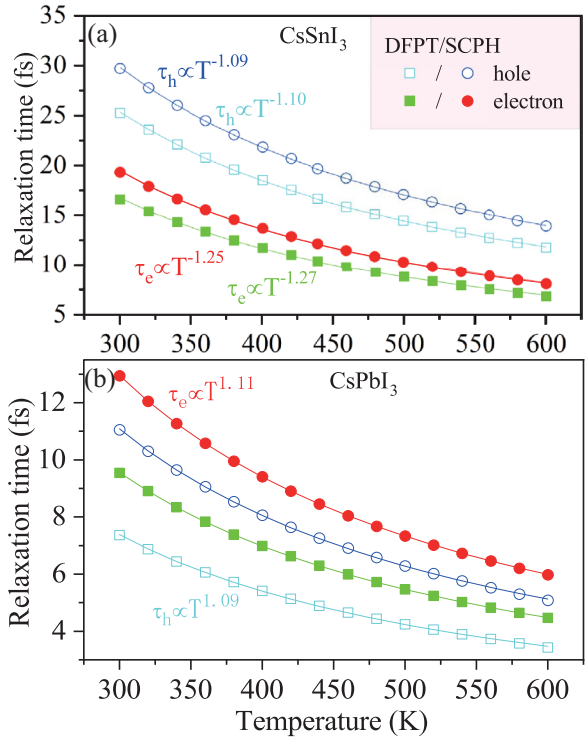

FIG. 5. Relaxation time of hole and electron carriers for (a) $CsSnI_3$ and (b) $CsPbI_3$, respectively. Curves are the fittings according to the power law.

crystal and consequently leads to the shifts of band edges [54,55], while LO modes couple to carriers via the polarization field, namely, the Fröhlich interaction [56,57]. To determine the dominant phonon mode in carrier scattering, we calculated the mode-resolved scattering rates for both halide perovskites, that is, the summation of the phonon mode in Eq. (3) is replaced by a specified mode. As shown in Fig. 6, we plotted the logarithmic-scaled scattering rates versus temperature for five longitudinal modes of both halide perovskites. The collective atom motions of the LO modes have been schematically plotted in Figs. 3(c)–3(f) and discussed in Sec. III A. For $CsSnI_3$, it is found that the LO_4 mode predominantly contributes to the scattering rates, with typical rates of $\sim$1–10 ps^{-1} for the hole and electron carriers, as shown in Figs. 6(a) and 6(b). This indicates that the stretching motion of the Sn-I bonds does greatly affect the carrier transport via the Fröhlich interaction. We have calculated the Born effective charges of halide perovskites to verify the large polarization field in the halide perovskites, as listed in Table I. It is found that I and Sn atoms have large Born effective charges, i.e., $Z^{*\parallel}_{I} = -5.41$ and $Z^{*}_{Sn} = 5.78$. The large anisotropy of the Born effective charge of the I atom indicates that the polarization field is mainly along the Sn-I bond, which couples to carriers via the Fröhlich interaction. Since carriers transport mainly through the bands formed by $5p$ orbits of Sn and I, it can be expected that the stretching motion of the Sn-I bond will heavily scatter the carriers in the highest valence band (HVB) and lowest valence band (LCB).

Recently, experiments on the photoluminescence of lead halide perovskites [58–61] have revealed that hot carriers are mainly cooled by coupling to the LO mode with energy of 15.0 meV (about the frequency of 121 cm^{-1}). Note that the frequency of the LO_4 mode at the Γ point takes 131 and 117 cm^{-1} for $CsSnI_3$ and $CsPbI_3$, respectively, which is in good agreement with the experiment results [58–61]. In comparison, the Cs atom has smaller Z^*, indicating weaker

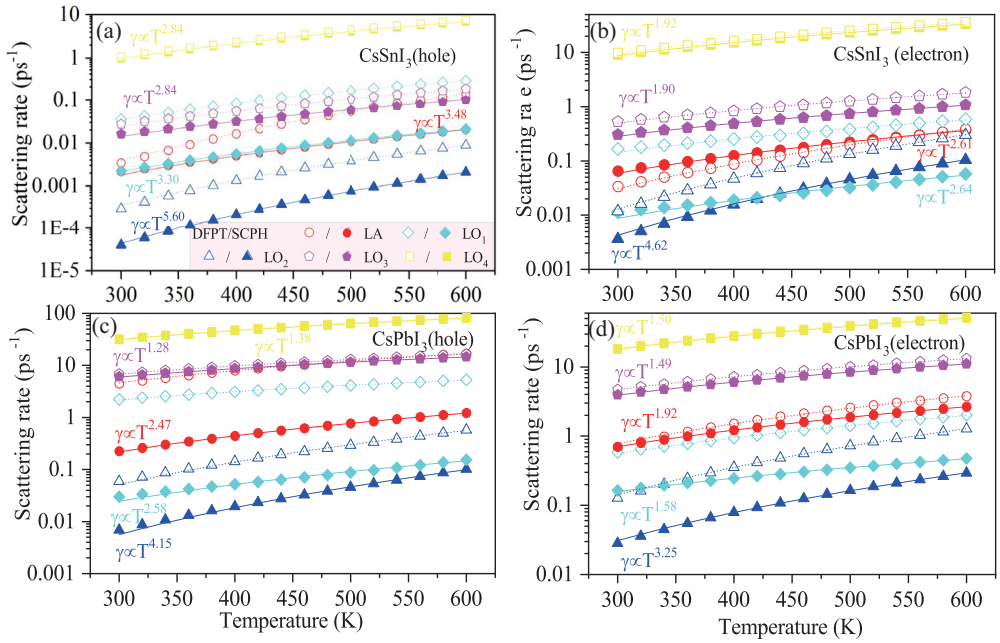

FIG. 6. (a),(b) Mode-resolved scattering rates for (a) hole and (b) electron carriers of $CsSnI_3$. (c),(d) Mode-resolved scattering rates for (c) hole and (d) electron carriers of $CsPbI_3$. Open symbols represent the scattering rates scattered by the harmonic phonon (DFPT), while the solid symbols mark the rates scattered by the anharmonic phonon (SCPH). Curves are the fittings according to the power law.

polarization for the rattling motions. Indeed, the scattering rate contributed by the rattling mode only accounts for a thousandth rate of the bond stretching mode for both carriers at 300 K. It is noticed that the LO_2 mode contributes the least scattering rate compared with other longitudinal modes. This means that the distortion of octahedron SnI_6 does not significantly affect the carrier mobilities since it does not vary the length of the Sn-I bond. Also, the longitudinal acoustic mode LA contributes a trivial scattering rate compared with the LO_4 mode, which is consistent with the experiment results [58]. It is noticed that the scattering rates of low-frequency modes, i.e., LO_1 and LO_2, have decreased significantly after the renormalization of the interatomic forces. However, the scattering rate of high-frequency mode LO_4 only decreases a little. For the LO_4 mode, the scattering rate of holes at 300 K decreases by 7% when the quartic anharmonicity is included. This leads to the enhancement of mobility for hole carriers after the renormalization of the interatomic force. As the temperature increases, the rates increases in the power law $\gamma = aT^{\eta}$. For $CsSnI_3$, the exponent η usually decreases as the frequencies of the LO modes increase, and hole carriers have larger η than the electron carriers.

Similar to $CsSnI_3$, the carrier scattering rate of $CsPbI_3$ predominantly comes from the LO_4 mode, as shown in Figs. 6(c) and 6(d). For hole carriers, the scattering rate of LO_4 at 300 K is one order larger than that of $CsSnI_3$. Besides the LO_4 mode, the contribution of the LO_3 mode accounts for 20% of the total scattering rate, indicating another important scattering source. Due to strong scattering, the exponents η of $CsPbI_3$ are significantly lower than those of $CsSnI_3$ accordingly. When the quartic anharmonicity is included, the scattering rates decrease significantly for those low-frequency modes, similar to the case of $CsSnI_3$.

Experimentally, the slow relaxation time of hot carriers has been observed in halide perovskites by photoluminescence spectra [17–19]. Hot carriers were excited by photons with energy of 3.1 eV and the relaxation time lasted 0.4 ps for holes and electrons [18,19]. To explore the origin of slow relaxation time, we calculated the k-dependent scattering rates at 300 K for both HVB and LCB, as plotted in Fig. 7. For $CsSnI_3$, the band scattering rates show deep valleys at the point R and they nearly overlap each other along the k-path $\overline{MRZ}$, as shown in Fig. 7(a). Near the band edge, the band scattering rates contributed by the LO_4 mode almost overlap with the total rates, indicating the dominant role of LO_4 in carrier scattering. Similar behaviors have also been found in $CsPbI_3$, as shown in Fig. 7(b). Nevertheless, the scattering valley is much deeper in $CsPbI_3$ than that in $CsSnI_3$, indicating a longer relaxation time of hot carriers for the former. Taking $CsPbI_3$ as an example, we can estimate the relaxation time of hot carriers for lead halide perovskites in the experimental measurements. Electrons in the valence bands will be pumped into the conduction bands near the M point without the momentum variation after absorbing the photons of $h\nu = 3.1$ eV, as shown in the inset of Fig. 7(b). By continuously exciting LO_4 phonons of $\hbar\omega = 15.0$ meV, the hot electron and hole will lose the energy of 0.76 and 0.60 eV, respectively, before relaxing into the band edges. Taking the middle point value as the average scattering rate ($\bar{\gamma} = 110$ ps^{-1}), the average time interval is estimated to be 9 fs ($\Delta t = 1/\bar{\gamma}$) for hot carriers to emit one LO_4 phonon.

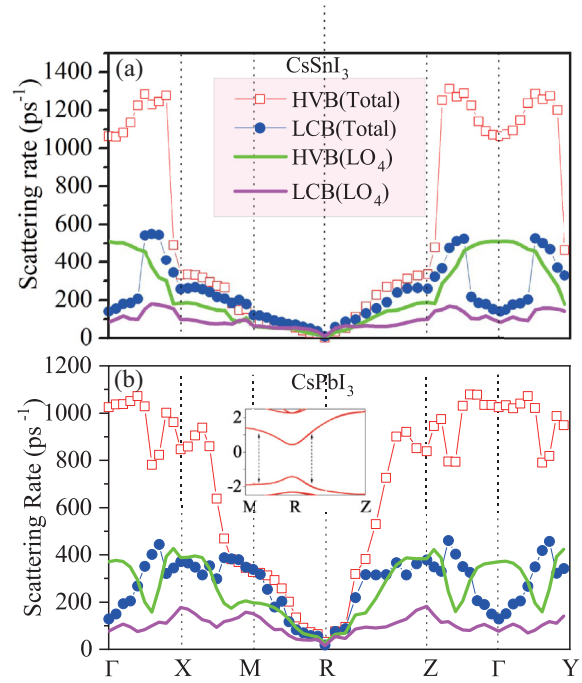

FIG. 7. Band scattering rates for the HVB and LCB of (a) $CsSnI_3$ and (b) $CsPbI_3$ at 300 K. Rates contributed by total modes (lines with symbols) and LO_4 mode (lines) are both presented. Inset: Schematic plot of electron hopping from HVB to LCB by adsorbing the photon of 3.1 eV.

The relaxation time is estimated to be 0.45 and 0.36 ps for hot electrons and holes, respectively, in good agreement with the experiment results [18,19].

D. Electron-phonon coupling strength

As we have discussed above, the LO_4 mode plays an important role in the carrier scattering for halide perovskites. It is instructive to explore the origin of carrier scattering from the EPC strength. In a small electric field, carriers are mainly scattered into new states within the same band, that is, the intraband scattering is predominant in carrier transport. Thus, we calculated the mode-resolved intraband EPC strength for both the HVB and LCB, as shown in Fig. 8. The phonon dispersions have been renormalized at 400 K by the SCPH method to include the quartic anharmonicity in the EPC calculations. Since the EPC strength in Eq. (4) is both k and q dependent, we have averaged the strength over the q mesh of $20 \times 20 \times 20$ in the Brillouin zone so that it is only k dependent. For the HVB of $CsSnI_3$, the EPC strength of LO_4 far exceeds those of other modes, showing a plateau with the typical value of 30 meV along the k path, as shown in Fig. 8(a). At the point R, EPC strength of LO_4 reaches 29.8 meV, which is about six times larger than those of other modes. As expected, the LO_2 mode has the lowest EPC strength, consistent with its least scattering rate in $CsSnI_3$. Interestingly, the EPC strengths show dips at the point R for the HVB of $CsSnI_3$, indicating a weakened carrier scattering at the band edge. When the interatomic forces are renormalized, the EPC strengths have decreased significantly for the low-frequency modes,

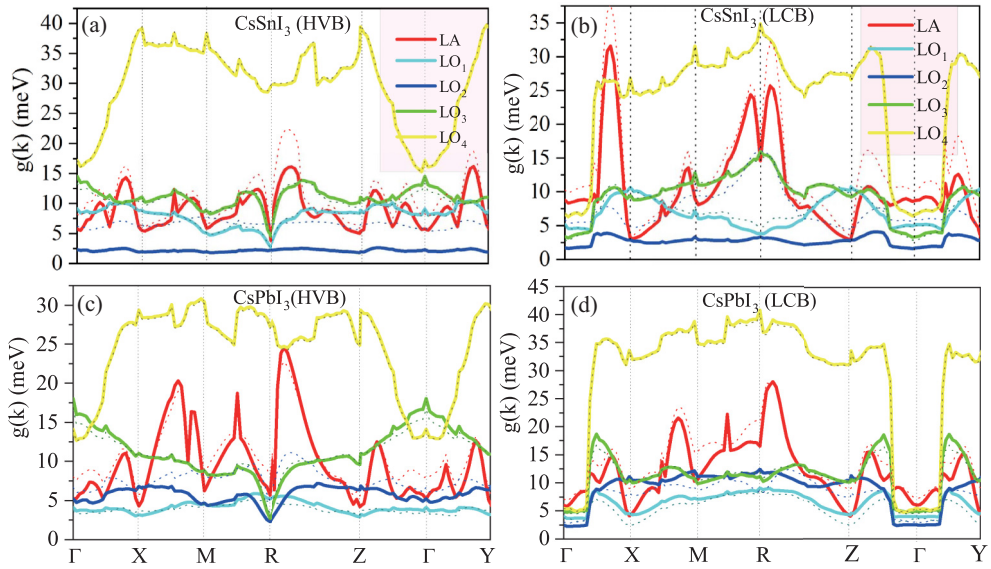

FIG. 8. (a),(b) Mode-resolved intraband EPC strengths along the k path for the (a) HVB and (b) LCB of $CsSnI_3$. (c),(d) Mode-resolved intraband EPC strengths along the k path for the (c) HVB and (d) LCB of $CsPbI_3$. The dotted and solid lines represent the EPC strengths calculated from harmonic and anharmonic phonons (renormalized at 400 K), respectively.

i.e., LA, LO_1, and LO_2, while the strength of LO_4 remains nearly unchanged, with the variation less than 1%. Due to the strong stiffening of low-frequency modes, it is expected that the EPC strengths will decrease significantly after the renormalization. In comparison, the high-frequency modes have been little stiffened, giving rise to nearly unchanged EPC strengths. Compared with the case of HVB, the EPC strengths of LCB have been enhanced significantly at the R point for the LA, LO_3, and LO_4 modes, as shown in Fig. 8(b). Similarly, the LO_2 mode has lowest coupling strength at the R point, indicating a trivial scattering effect for the distortion of the octahedron SnI_6.

Similar to the case of $CsSnI_3$, the EPC strength of the LO_4 mode also exhibits a plateau for the HVB of $CsPbI_3$, which indicates a strong coupling to hole carriers, as shown in Fig. 8(c). Abrupt dips of the EPC strengths emerge at the R point when the HVB couples to the phonon modes rather than LO_4. For the LCB of $CsPbI_3$, the EPC strengths are enhanced overall at the point R and no dips are observed, indicating an enhancement of electron scattering.

Furthermore, we calculated the derivative of the Kohn-Sham potential with respect to the displacements of longitudinal optical modes at the R point for both halide perovskites. The collective atomic displacement A was set to be 0.01 Å and the ground state without atomic displacements was used as the reference. The atoms in the unit cell were displaced along the phonon eigenvectors with the magnitudes proportional to the projected probability. Namely, for a phonon mode with the eigenvector $\phi_{q,\nu} = \sum_{l,\alpha} c_l^\alpha e^{i(\mathbf{q}\cdot\mathbf{R}_l - \nu t)}$, we displaced the atom l along the direction α by $u_l^\alpha = A|c_l^\alpha|^2$ and calculated the deformation potential by $\Delta E/A$. Our calculation results reveal that $\partial V_{KS}/\partial \mathbf{u}_{R\nu}$ takes 0.102 (0.183), 0.041 (0.081), 0.02 (0.023), and 0.005 (0.024) mRy/Å for $CsSnI_3$ ($CsPbI_3$) as the mode index ν counts from LO_4 to LO_1. Therefore, the large EPC strength of the LO_4 mode originates from the large deformation potential, so that carriers in $CsPbI_3$ couple more strongly to the LO_4 mode than those in $CsSnI_3$.

IV. CONCLUSIONS

We have investigated the effect of quartic anharmonicity on the transporting properties of halide perovskites by first-principles calculations. The hybrid functional of HSE06 has been employed to get accurate band gaps and the effective carrier mass is calculated. The self-consistent phonon calculations indicate that the interatomic forces have been significantly strengthened and the low-frequency modes have been stiffened by including the quartic anharmonicity. Our results reveal that when the quartic anharmonicity of lattices is considered in the EPC calculations, the hole mobility takes 595.9 and 84.5 cm^2/Vs, in good agreement with the experiment results. By calculating the mode-resolved scattering rates, it is found that the stretching mode of the Sn-I (Pb-I) bonds with typical frequency values of 120 cm^{-1} is predominant in the carrier scattering. The high scattering rates can be attributed to the Fröhlich interaction between carriers and the polarization field. The band scattering rates of HVB and LCB overlap each other and show abrupt dips at the band edges, indicating a slow relaxation of hot carriers. By calculating the mode-resolved intraband EPC strengths along the k path in the Brillouin zone, we find that the LO_4 mode has the largest EPC strength due to its high derivative of potential with respect to the displacements of the phonon modes. Compared with the EPC strengths calculated within the approximation of the harmonic phonon, the quartic anharmonicity leads to smaller EPC strengths for the low-frequency modes, which results in the reduction of carrier scattering in halide perovskites. We hope that our results can benefit future research on the transporting properties of halide perovskites.

ACKNOWLEDGMENTS

This work is supported by National Natural Science Foundation of China (Grants No. 11504027, No. 51961031, No. 51541105). K.-C.Z. acknowledges funding support from the LiaoNing Revitalization Talents Program (Grant No. XLYC2007120). Y.L. acknowledges the support from the Science Foundation of Hebei Province (Grant No. A2015203021) and Key Project of Hebei Educational Department, China (Grant No. ZD2018015).

[1] S. Stranks and H. Snaith, Nat. Nanotechnol. **10**, 391 (2015).
[2] L. Lei, Q. Dong, K. Gundogdu, and F. So, Adv. Funct. Mater. **31**, 2010144 (2021).
[3] A. Kojima, K. Teshima, Y. Shirai, and T. Miyasaka, J. Am. Chem. Soc. **131**, 6050 (2009).
[4] F. Qiu, J. Sun, Z. Zhang, T. Shen, H. Liu, and J. Qi, Mater. Today Energy **21**, 100837 (2021).
[5] I. Chung, J.-H. Song, J. Im, J. Androulakis, C. D. Malliakas, H. Li, A. J. Freeman, J. T. Kenney, and M. G. Kanatzidis, J. Am. Chem. Soc. **134**, 8579 (2012)
[6] L. Y. Huang and W. R. L. Lambrecht, Phys. Rev. B **90**, 195201 (2014).
[7] Q. Tai and F. Yan, Adv. Mater. **29**, 1700192 (2017)
[8] S. Liu, Y. Guan, Y. Sheng, Y. Hu, Y. Rong, A. Mei, and H. Han, Adv. Energy Mater. **10**, 1902492 (2020).
[9] Y. Wang, G. Chen, D. Ouyang, X. He, C. Li, R. Ma, W.-J. Yin, and W. C. H. Choy, Adv. Mater. **32**, 2000186 (2020).
[10] A. Marronnier, H. Lee, B. Geffroy, J. Even, Y. Bonnassieux, and G. Roma, J. Phys. Chem. Lett. **8**, 2659 (2017).
[11] R. X. Yang, J. M. Skelton, E. L. da Silva, J. M. Frost, and A. Walsh, J. Phys. Chem. Lett. **8**, 4720 (2017)
[12] H. Xie, S. Hao, J. Bao, T. J. Slade, G. J. Snyder, C. Wolverton, and M. G. Kanatzidis, J. Am. Chem. Soc. **142**, 9553 (2020).
[13] W. Lee and H. Li, A. B. Wong and P. Yang, Proc. Natl. Acad. Sci. USA **114**, 8693 (2017)
[14] Y. Chen, Y. Lei, Y. Li, Y. Yu, J. Cai, M.-H. Chiu, R. Rao, Y. Gu, C. Wang, W. Choi, H. Hu, C. Wang, Y. Li, J. Song, J. Zhang, B. Qi, M. Lin, Z. Zhang, A. E. Islam, B. Maruyama *et al.* Nature (London) **577**, 209 (2020)
[15] Y. Zhao, C. Lian, S. Zeng, Z. Dai, S. Meng, and J. Ni, Phys. Rev. B **101**, 184303 (2020)
[16] T. Tadano and S. Tsuneyuki, Phys. Rev. Lett. **120**, 105901 (2018).
[17] M. Li, J. Fu, Q. Xu, and T. C. Sum, Adv. Mater. **31**, 1802486 (2019).
[18] G. Xing, N. Mathews, S. Sun, S. S. Lim, Y. M. Lam, M. Gräzel, S. Mhaisalkar, and T. C. Sum, Science **342**, 344 (2013).
[19] T. C. Sum, N. Mathews, G. Xing, S. S. Lim, W. K. Chong, D. Giovanni, and H. A. Dewi, Acc. Chem. Res. **49**, 294 (2016).
[20] G. Grancini, M. Maiuri, D. Fazzi, A. Petrozza, H. J. Egelhaaf, D. Brida, G. Cerullo, and G. Lanzani, Nat. Mater. **12**, 29 (2013).
[21] J. Yang, X. Wen, H. Xia, R. Sheng, Q. Ma, J. Kim, P. Tapping, T. Harada, T. W. Kee, F. Huang, Y.-B. Cheng, M. Green, A. Ho-Baillie, S. Huang, S. Shrestha, R. Patterson, and G. Conibeer, Nat. Commun. **8**, 14120 (2017).
[22] M. Achermann, A. P. Bartko, J. A. Hollingsworth, and V. I. Klimov, Nat. Phys. **2**, 557 (2006).
[23] J. Heyd, G. E. Scuseria, and M. Ernzerhof, J. Chem. Phys. **118**, 8207 (2003)
[24] S. Poncé, E. R. Margine, and F. Giustino, Phys. Rev. B **97**, 121201(R) (2018).
[25] F. Giustino, Rev. Mod. Phys. **89**, 015003 (2017)
[26] X. Gonze and C. Lee, Phys. Rev. B **55**, 10355 (1997).
[27] J. Noffsinger, F. Giustino, B. D. Malone, C.-H. Park, S. G. Louie, and M. L. Cohen, Comput. Phys. Commun. **181**, 2140 (2010).
[28] A. A. Mostofi, J. R. Yates, Y.-S. Lee, I. Souza, D. Vanderbilt, and N. Marzari, Comput. Phys. Commun. **178**, 685 (2008).
[29] T. Tadano and S. Tsuneyuki, Phys. Rev. B **92**, 054301 (2015).
[30] N. R. Werthamer, Phys. Rev. B **1**, 572 (1970)
[31] F. Zhou, W. Nielson, Y. Xia, and V. Ozolins, Phys. Rev. Lett. **113**, 185501 (2014)
[32] R. Car and M. Parrinello, Phys. Rev. Lett. **55**, 2471 (1985).
[33] D. J. Evans and B. L. Holian, J. Chem. Phys. **83**, 4069 (1985).
[34] P. Giannozzi, S. Baroni, N. Bonini, M. Calandra, R. Car, C. Cavazzoni, D. Ceresoli, G. L. Chiarotti, M. Cococcioni, I. Dabo, A. D. Corso, S. de Gironcoli, S. Fabris, G. Fratesi, R. Gebauer, U. Gerstmann, C. Gougoussis, A. Kokalj, M. Lazzeri, L. Martin-Samos, A. P Seitsonen, and P. Umari, J. Phys.: Condens. Matter **21**, 395502 (2009).
[35] D. R. Hamann, Phys. Rev. B **88**, 085117 (2013).
[36] J. P. Perdew, K. Burke, and M. Ernzerhof, Phys. Rev. Lett. **77**, 3865 (1996).
[37] S. Maintz, V. L. Deringer, A. L. Tchougréeff, and R. Dronskowski, J. Comput. Chem. **37**, 1030 (2016).
[38] J. Liu, A. E. Phillips, D. A. Keen, and M. T. Dove, J. Phys. Chem. C **123**, 14934 (2019)
[39] X. Shen, Y. Zhang, S. V. Kershaw, T. Li, C. Wang, X. Zhang, W. Wang, D. Li, Y. Wang, M. Lu, L. Zhang, C. Sun, D. Zhao, G. Qin, X. Bai, W. W. Yu, and A. L. Rogach, Nano Lett. **19**, 1552 (2019).
[40] Y. J. Lee, J. S. Han, D. E. Lee, T. H. Lee, J. Y. Kim, J. M. Suh, J. H. Lee, I. H. Im, S. J. Kim, K. J. Kwak, and H. W. Jang, Adv. Electron. Mater. **8**, 2100624 (2022).
[41] S. Sarkar, S. Banerjee, A. Swarnkar, and P. Mandal, J. Phys. Chem. C **125**, 10539 (2021)
[42] S. Dastidar, S. Li, S. Y. Smolin, J. B. Baxter, and A. T. Fafarman, ACS Energy Lett. **2**, 2239 (2017)
[43] M. Badrooj, F. Jamali-Sheini, and N. Torabi, J. Phys. Chem. C **124**, 27136 (2020)
[44] N. Giesbrecht, J. Schlipf, I. Grill, P. Rieder, V. Dyakonov, T. Beina, A. Hartschuh, P. Muller-Buschbaumb, and P. Docampo, J. Mater. Chem. A **6**, 4822 (2018)
[45] S. Ponce, M. Schlipf, and F. Giustino, ACS Energy Lett. **4**, 456 (2019).
[46] R. L. Milot, G. E. Eperon, H. J. Snaith, M. B. Johnston, and L. M. Herz, Adv. Funct. Mater. **25**, 6218 (2015)
[47] M. Karakus, S. A. Jensen, F. D'Angelo, D. Turchinovich, M. Bonn, and E. Canovas, J. Phys. Chem. Lett. **6**, 4991 (2015).

[48] H. T. Yi, X. Wu, X. Zhu, and V. Podzorov, Adv. Mater. **28**, 6509 (2016).
[49] Y. Wang, Z. Wan, Q. Qian, Y. Liu, Z. Kang, Z. Fan, P. Wang, Y. Wang, C. Li, C. Jia, Z. Lin, J. Guo, I. Shakir, M. Goorsky, X. Duan, Y. Zhang, Y. Huang, and X. Duan, Nat. Nanotechnol. **15**, 768 (2020)
[50] T. Liu, W. Tang, S. Luong, and O. Fenwick, Nanoscale **12**, 9688 (2020)
[51] Z. Chen, L. Dong, H. Tang, Y. Yu, L. Ye, and J. Zang, CrystEngComm **21**, 1389 (2019).
[52] K. Shum, Z. Chen, J. Qureshi, C. Yu, J. J. Wang, W. Pfenninger, N. Vockic, J. Midgley, and J. T. Kenney, Appl. Phys. Lett. **96**, 221903 (2010).
[53] L. Y. Huang and W. R. L. Lambrecht, Phys. Rev. B **88**, 165203 (2013).
[54] K.-C. Zhang, L.-Y. Cheng, C. Shen, Y.-F. Li, Y. Liu, and Y. Zhu, Phys. Chem. Chem. Phys. **23**, 18869 (2021).
[55] L.-Y. Cheng, K.-C. Zhang, Y.-F. Li, Y. Liu, and Y. Zhu, J. Alloys Compd. **894**, 162542 (2022).
[56] C. M. Iaru, A. Brodu, N. J. J. van Hoof, S. E. T. ter Huurne, J. Buhot, F. Montanarella, S. Buhbut, P. C. M. Christianen, D. Vanmaekelbergh, C. de M. Donega, J. G. Rivas, P. M. Koenraad, and A. Y. Silov, Nat. Commun. **12**, 5844 (2021)
[57] C. Verdi and F. Giustino, Phys. Rev. Lett. **115**, 176401 (2015)
[58] A. D. Wright, C. Verdi, R. L. Milot, G. E. Eperon, M. A. Pérez-Osorio, H. J. Snaith, F. Giustino, M. B. Johnston, and L. M. Herz, Nat. Commun. **7**, 11755 (2016).
[59] D. Zhao, H. Hu, R. Haselsberger, R. A. Marcus, M.-E. Michel-Beyerle, Y. M. Lam, J.-X. Zhu, C. La-o-vorakiat, M. C. Beard, and E. E. M. Chia, ACS Nano **13**, 8826 (2019).
[60] J. Fu, Q. Xu, G. Han, B. Wu, C. H. A. Huan, M. L. Leek, and T. C. Sum, Nat. Commun. **8**, 1300 (2017)
[61] S. Sourabh, V. R. Whiteside, I. R. Sellers, Y. Zhai, K. Wang, M. C. Beard, V. Yeddu, M. T. Bamidele, and D. Y. Kim, Phys. Rev. Mater. **5**, 095402 (2021).